Article

Automated discovery of reprogrammable nonlinear dynamic metamaterials

Giovanni Bordiga [1], Eder Medina [1,2], Sina Jafarzadeh [1,3], Cyrill Bösch [1,4], Ryan P. Adams [2], Vincent Tournat [1,5] & Katia Bertoldi [1]✉

Harnessing the rich nonlinear dynamics of highly deformable materials has the potential to unlock the next generation of functional smart materials and devices. However, unlocking such potential requires effective strategies to spatially engineer material architectures within the nonlinear dynamic regime. Here we introduce an inverse-design framework to discover flexible mechanical metamaterials with a target nonlinear dynamic response. The desired dynamic task is encoded via optimal tuning of the full-scale metamaterial geometry through an inverse-design approach powered by a fully differentiable simulation environment. By deploying such a strategy, mechanical metamaterials are tailored for energy focusing, energy splitting, dynamic protection and nonlinear motion conversion. Furthermore, our design framework can be expanded to automatically discover reprogrammable architectures capable of switching between different dynamic tasks. For instance, we encode two strongly competing tasks— energy focusing and dynamic protection—within a single architecture, using static precompression to switch between these behaviours. The discovered designs are physically realized and experimentally tested, demonstrating the robustness of the engineered tasks. Our approach opens an untapped avenue towards designer materials with tailored robotic-like reprogrammable functionalities.

Effective control over the nonlinear behaviour of material structures is essential for various dynamic tasks, including energy harvesting from elastic pulses, impact mitigation and mechanical signal processing. Mechanical metamaterials—artificially engineered materials with mechanical responses determined by structure rather than composition—have emerged as a promising platform to achieve such control. By carefully arranging specially designed building blocks in space, these metamaterials have demonstrated complex functionalities such as focusing[1], executing mathematical operations[2,3] and cloaking objects[4–6]. However, most of the proposed designs operate in the linear regime and are optimized for a single functionality.

Recent advancements have highlighted the enormous potential of flexible metamaterials in controlling nonlinear waves[7,8]. By leveraging their ability to undergo large deformations, exploit instabilities and navigate multi-welled energy landscapes, these systems have demonstrated capabilities such as unidirectional signal propagation[9], long-range propagation even in the presence of dissipation[10] and impact mitigation[11]. Nevertheless, the exploration and rational control of nonlinear dynamics in flexible mechanical materials is still in its early stages, with most studies focused on periodic systems. Designing periodic material structures inherently restricts our ability to manipulate energy flow through space and time. While it has been shown that defects can lead to diverse transmission pathways in the underlying lattice[12], the placement of these defects has relied on intuition rather than systematic approaches. By transitioning to automated design strategies, it may be possible to unlock new two-dimensional (2D)

[1]John A. Paulson School of Engineering and Applied Sciences, Harvard University, Cambridge, MA, USA. [2]Department of Computer Science, Princeton University, Princeton, NJ, USA. [3]Department of Energy Conversion and Storage, Technical University of Denmark, Lyngby, Denmark. [4]Institute of Geophysics, ETH Zurich, Zurich, Switzerland. [5]Laboratoire d'Acoustique de l'Université du Mans (LAUM), Institut d'Acoustique - Graduate School (IA-GS), Le Mans Université, CNRS, Le Mans, France. ✉e-mail: bertoldi@seas.harvard.edu
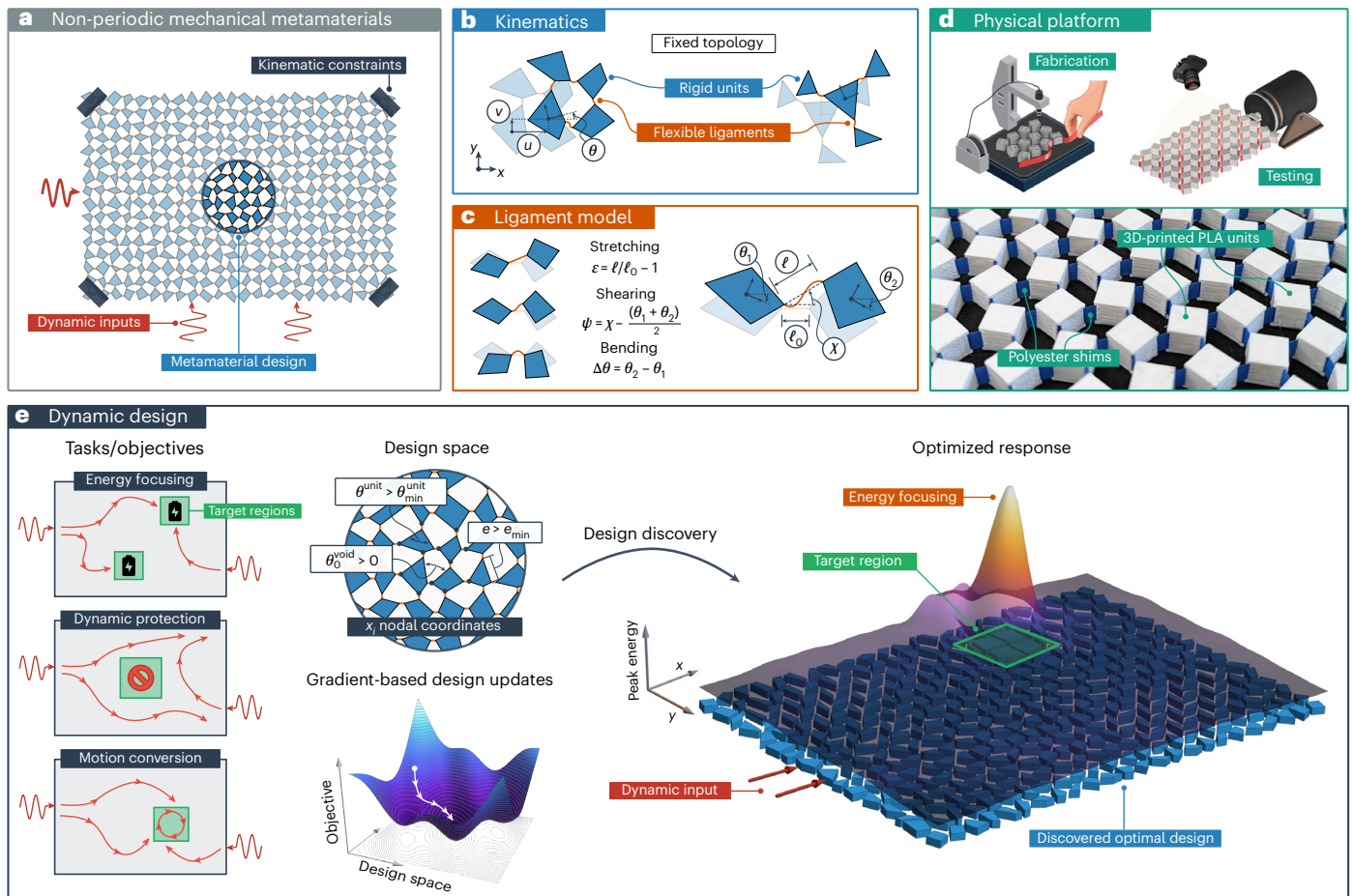
Fig. 1 | Automated design of reprogrammable nonlinear dynamic metamaterials. a, We focus on 2D flexible mechanical metamaterials comprising a network of rigid units connected by flexible ligaments. **b,c**, Assuming a fixed topology for the connections, the dynamic behaviour of the system is governed by the rigid-body kinematics of the units (**b**) and the mechanical response of the flexible ligaments (**c**). **d**, The metamaterials are physically realized via 3D printing of PLA units connected by thin flexible plastic shims. **e**, Given a high-level description of the dynamic tasks (for example, energy focusing at target locations, protection, motion conversion), the design space of non-periodic geometries is explored efficiently through the use of adjoint gradients and a gradient-based optimizer while taking fabrication constraints into account (that is, lower bounds on the void angle between adjacent units θ_0^{void}, the solid angle of the unit θ^{unit} and the edge length of the unit e).

architectures that can achieve unprecedented control over energy flow in the nonlinear regime[13].

Optimization is an attractive principle for automated design, and it has been largely successful in the identification of metamaterials with desired mechanical responses. Despite the well-known limitation of local convergence and the additional computational cost of calculating gradients, gradient-based approaches have been extensively applied to structural design problems[14-18]. For instance, in the linear regime, gradient-based optimization has yielded material structures exhibiting a maximized relative size of bandgaps[19,20], negative effective properties[21,22], directional wave propagation[23], mode shaping of flexural waves[24], topologically protected modes[25], minimal dynamic compliance[26], maximized stiffness in fibre-reinforced composites[27] and mechanism-like deformations[28], among others. However, in the nonlinear regime, significantly less progress has occurred, with efforts mostly focused on the use of gradient-free algorithms and machine learning approaches. Gradient-free methods based on stochastic search[29,30] and Bayesian optimization[31,32] have shown effectiveness in exploring the complex energy landscape of flexible metamaterials in the static regime. Yet such approaches do not scale to problems involving expensive forward simulations or a large number of design parameters[33]. Similar limitations are faced by approaches based on machine learning techniques since they require a large database of simulations to train a surrogate model of the forward response and then optimize over the fast surrogate[34-37]. On the other hand, gradient-based optimization, despite being locally convergent, has shown promise when combined with large parameter spaces in discovering underlying patterns and behaviours[38-40]. Furthermore, automatic differentiation (AD), commonplace in the machine learning field[41], has facilitated the calculation of exact gradients[42-45]. In mechanics, the additional information provided by gradients has proved effective in guiding the design of elasto-plastic structures for failure resistance under impact[46], tuning Poisson's ratio at finite strains[47], optimizing nonlinearly resonant frame structures[48,49] and discovering shape-morphing cellular solids[50]. Although these works indicate the great potential of gradient-based optimization for nonlinear problems, the rich space of dynamical behaviours, especially transient behaviour, in nonlinear mechanical metamaterials remains relatively unexplored[29].

Here we introduce a framework to automate the design of flexible metamaterial structures that can execute desired nonlinear dynamic tasks and whose functionality can be reprogrammed on the fly. In particular, we focus on 2D flexible mechanical metamaterials comprising a network of rigid units connected by flexible ligaments (Fig. 1a–d), which have gained significant attention due to their ability to exhibit a negative effective Poisson's ratio[51,52] and a wide range of target static nonlinear mechanical responses[53-56], and to support the propagation of solitary

pulses[57,58]. By leveraging recent advancements in AD[42–45], we demonstrate how the nonlinear dynamic response of these metamaterials can be tailored to execute complex tasks such as energy focusing, energy splitting, dynamic protection and nonlinear motion conversion (Fig. 1e). Additionally, we extend the design framework to create architectures capable of seamlessly switching between different tasks. As an example, we encode two strongly competing tasks—energy focusing and dynamic protection—within a single architecture and harness static precompression to switch between these behaviours. To demonstrate the robustness of the engineered tasks, the discovered designs are physically realized and tested. All together, the results presented here highlight the efficacy of our framework in enabling the non-electronic encoding of reprogrammable nonlinear dynamic tasks in artificial material structures.

Design strategy

To rationally design 2D flexible mechanical metamaterials with target nonlinear dynamic responses, we developed a fully differentiable simulation environment that leverages AD tools[42,43]. This approach automates the derivation of the equations of motion from an energy functional and, therefore, greatly simplifies the modelling and simulation process. Furthermore, it facilitates the inverse design of metamaterials by automatically computing gradients of the solution with respect to any design parameter. Our design strategy consists of the following four steps.

Derivation and solution of equations of motion

The response of 2D flexible mechanical metamaterials comprising a network of rigid units connected by flexible ligaments can be captured using a discrete model comprising rigid units connected at their vertices by a combination of elastic springs[54,59] (Fig. 1a–c). In particular, the strain energy of the ith ligament is assumed to be of the form

$$\mathcal{V}_i = \frac{1}{2}\left[k_\ell(\varepsilon_i \ell_i^0)^2 + k_\theta \Delta\theta_i^2 + k_s(\psi_i \ell_i^0)^2 \right] + \mathcal{V}_i^c, \tag{1}$$

where k_ℓ, k_θ and k_s denote the stiffness of the ligament upon stretching, bending and shearing, respectively. Moreover, $\varepsilon_i = \ell_i/\ell_i^0 - 1$, with ℓ_i and ℓ_i^0 being the deformed and rest length of the ith ligament, respectively; $\Delta\theta_i = \theta_i^{(2)} - \theta_i^{(1)}$, with $\theta_i^{(1)}$ and $\theta_i^{(2)}$ being the rotation of the two units connected to the ligament; and $\psi_i = \chi_i - (\theta_i^{(1)} + \theta_i^{(2)})/2$, with χ_i being the angle between the deformed and undeformed configurations of the ligament (Fig. 1c). Finally, $\mathcal{V}_i^c$ is a differentiable contact model in the form of a strain energy term accounting for the contact between the rigid units connected by the ith ligament. Such contact energy is assumed to be of the form

$$\mathcal{V}_i^c = \frac{1}{2} k_c \left(\theta_i^{\text{void}} - \theta_{\text{cut-off}}\right)^2 \left(1 - \tau_i^2\right)^{-1} \mathcal{H}\left(\theta_{\text{cut-off}} - \theta_i^{\text{void}}\right), \tag{2}$$

where $\theta_i^{\text{void}} = \Delta\theta_i + \theta_{i,0}^{\text{void}}$ with $\theta_{i,0}^{\text{void}}$ being the rest void angle (Fig. 1e) and $\mathcal{H}$ denoting the Heaviside function. Moreover, k_c controls the initial stiffness of the contact, while the factor $(1 - \tau^2)^{-1}$, with $\tau = (\theta^{\text{void}} - \theta_{\text{cut-off}})/(\theta_{\text{cut-off}} - \theta_{\text{min}})$, introduces a vertical asymptote at $\theta^{\text{void}} = \theta_{\text{min}}$ to avoid compenetration. $\theta_{\text{cut-off}}$ and θ_{min} define the range of active contact with $\theta_{\text{cut-off}}$ being the upper limit and θ_{min}, the lower limit.

The Lagrangian of a metamaterial comprising N_h ligaments and N_u rigid units can then be written as

$$\mathcal{L} = \mathcal{T} - \mathcal{V} = \sum_{i=1}^{N_u} \mathcal{T}_i - \sum_{i=1}^{N_h} \mathcal{V}_i \tag{3}$$

where $\mathcal{V}_i$ is given by equation (1) and $\mathcal{T}_i$ denotes the kinetic energy of the ith rigid unit:

$$\mathcal{T}_i = \frac{1}{2}\left(\rho A_i \left(\dot{u}_i^2 + \dot{v}_i^2\right) + \rho I_i \dot{\theta}_i^2 \right), \tag{4}$$

where $\dot{u}_i$, $\dot{v}_i$ and $\dot{\theta}_i$ are the horizontal, vertical and rotational velocities of the centre of mass of the ith unit, and ρA_i and ρI_i denote the corresponding inertia (Fig. 1b). ρ denotes the mass per unit area, and A_i and I_i are the area and moment of area of the ith unit, respectively. We then take advantage of AD to take the partial derivatives of $\mathcal{L}$ with respect to all degrees of freedom of the metamaterial and obtain the equations of motion as

$$\frac{d}{dt}\frac{\partial \mathcal{L}}{\partial \dot{\mathbf{q}}} - \frac{\partial \mathcal{L}}{\partial \mathbf{q}} = \mathbf{f}_{\text{ext}}, \tag{5}$$

where t is time; $\mathbf{q} = \{u_1, v_1, \theta_1, \dots, u_{N_u}, v_{N_u}, \theta_{N_u}\}$ is a vector collecting the displacement components of all N_u units; and $\mathbf{f}_{\text{ext}}$ is the external force vector. Such an external loading function allows for modelling applied excitation $\mathbf{f}_{\text{app}}$ as well as dissipation $\mathbf{f}_{\text{damp}}$ so that $\mathbf{f}_{\text{ext}} = \mathbf{f}_{\text{app}} + \mathbf{f}_{\text{damp}}$. For the results shown in this work, we assume displacement-driven loading conditions, and hence $\mathbf{f}_{\text{app}} = 0$. Moreover, a simple linear viscous damping model is assumed so that $\mathbf{f}_{\text{damp}} = -C\dot{\mathbf{q}}$ with C being a diagonal matrix with translation and rotation damping coefficients c_u and c_θ, respectively. As equation (5) is a highly nonlinear system of ordinary differential equations, we numerically solve for the response $\mathbf{q}(t)$ using a Dormand–Prince explicit solver with adaptive step size[60] (see Supplementary Section 2a for more details).

Our simulation environment fully automates the derivation of equation (5) once all the energy functions (equations (1)–(4)) and external forcing ($\mathbf{f}_{\text{ext}}$) are defined as a function of all the relevant inputs. This approach provides the flexibility to change the geometry, topology and energy functions in a modular fashion.

Definition of the design space

Given that the behaviour of a mechanical metamaterial can be significantly altered by the shape of its rigid units[35], we choose here to use the shape of these rigid units as the design space. Such a design space can be parameterized via a vector $\mathbf{x}$ collecting the coordinates of vertices of the N_u rigid units in the undeformed (reference) configuration. To guarantee an identical mechanical response across all ligaments, the design space is constrained to maintain a constant rest length ℓ_0. The reference orientation of the ligaments is also kept constant during optimization. These constraints are enforced for the experimental convenience of characterizing a single set of hinge parameters, and are not fundamental limitations of our design framework. Furthermore, to both avoid infeasible designs and ensure manufacturability, we restrict the minimum edge length and vertex angle of the units, and constrain the void angle between neighbouring units to be positive (Supplementary Section 1 for additional details on the geometric parameterization and constraints).

Optimization

Finally, we pose the following question: how can we discover a geometry that can perform a desired dynamic task such as maximizing or minimizing the kinetic energy at target locations? By computing gradients with respect to the geometric parameters $\mathbf{x}$, it becomes possible to navigate a design space of much higher dimensionality than would be possible with a gradient-free method. For each dynamic task, we specify an objective function $J(\mathbf{q}(t), \mathbf{x})$ that reflects the efficacy of the geometry $\mathbf{x}$ in solving that task. Given any design $\mathbf{x}$, we numerically integrate equation (5) and then evaluate such objective function $J(\mathbf{q}(t), \mathbf{x})$. Furthermore, we take advantage of AD to compute its gradient as

$$\frac{dJ}{d\mathbf{x}} = \frac{\partial J}{\partial \mathbf{q}}\frac{\partial \mathbf{q}}{\partial \mathbf{x}} + \frac{\partial J}{\partial \mathbf{x}}, \tag{6}$$

where the response $\mathbf{q}(t)$ implicitly depends on the design $\mathbf{x}$ by means of the constraint imposed by equation (5). Note that the gradient term $\partial J/\partial \mathbf{x}$ is directly evaluated via AD, while the term $\frac{\partial J}{\partial \mathbf{q}}\frac{\partial \mathbf{q}}{\partial \mathbf{x}}$ is computed by
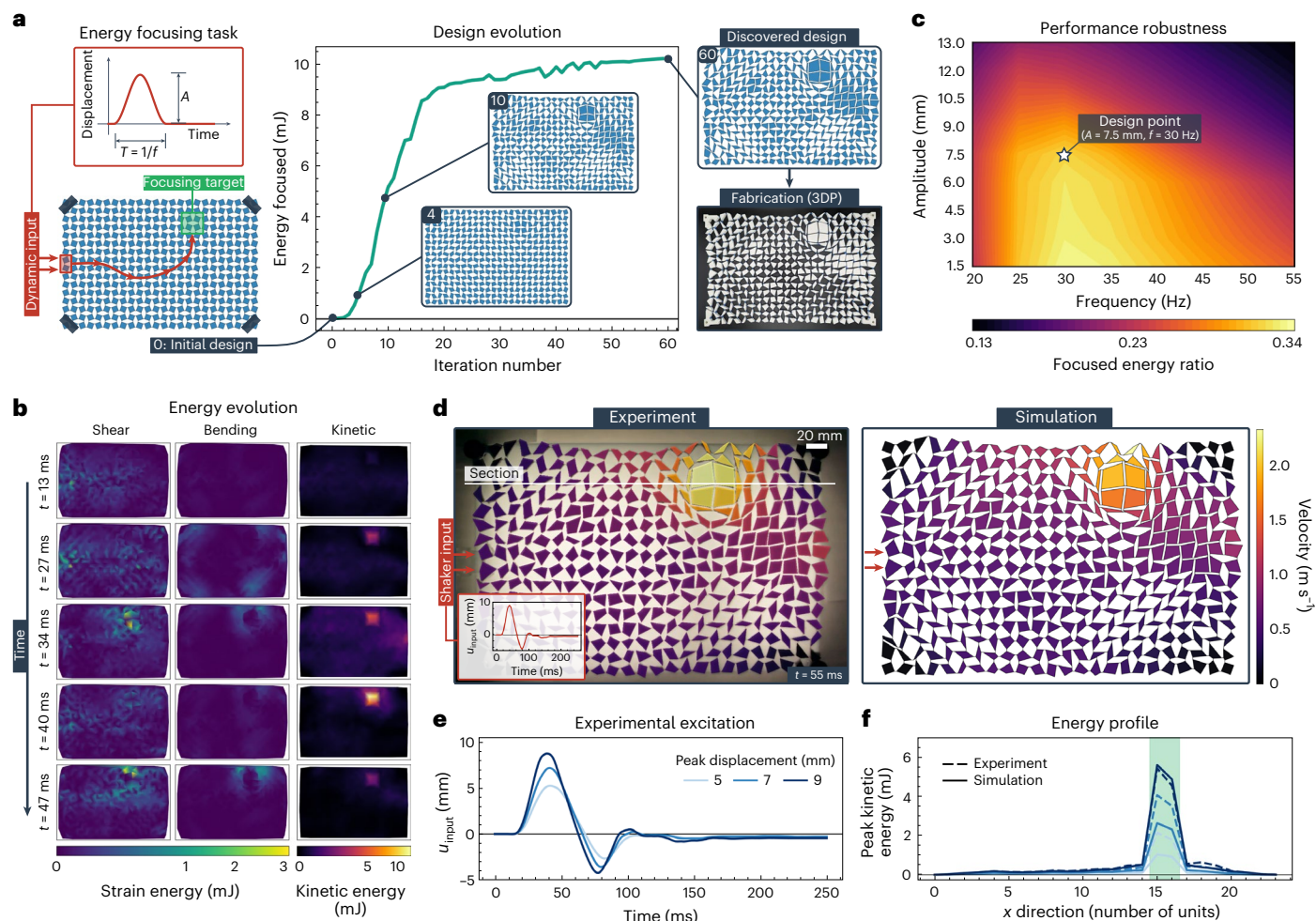
Fig. 2 | Energy focusing. a, The dynamic task of focusing the energy provided by a dynamic excitation on the left boundary of the system towards a target location is encoded in the metamaterial structure through our gradient-based design strategy. Left: a dynamic excitation in the form of pulse of period $T = f^{-1}$ is applied to the material domain and target region (in green) is selected for the focusing task. Right: the design evolution during optimization shows the effectiveness of the method in identifying the best direction in the huge design space of possible architectures (results shown for an input pulse with $A = 0.5s = 7.5$ mm and $f = 30$ Hz). The 60th design iteration is selected for fabrication and testing (3DP stands for 3D printing). **b**, Simulation snapshots of the spatial distribution of the most relevant energy components (shear, bending and kinetic) at $t = 13, 27, 34, 40$ and 47 ms. **c**, Contour plot of the simulated focused energy ratio (integrated kinetic energy of the target region compared with elsewhere, that is $J_{\Omega_t}/J_{\Omega \setminus \Omega_t}$) for the optimized design as a function of input frequency and amplitude predicting robustness with respect to the excitation away from the design point. **d**, Experimental (left) and numerical (right) snapshot of the velocity field at $t = 55$ ms for the optimized structure subject to the input shown in the inset. **e**, Additional experimental excitation signals used in the experiments. **f**, Corresponding evolution of the peak kinetic energy along the white line in **d**. The green shaded area denotes the target focusing region.

solving the adjoint problem associated with equation (5) using the same time integrator[60]. Finally, $dJ/d\mathbf{x}$ is passed to the optimizer to update the design $\mathbf{x}$ until convergence. To handle nonlinear constraints on the design space, required to ensure manufacturability (that is, lower bounds on the edge lengths and angles of the units), we adopt the Method of Moving Asymptotes[61] as the optimizer (provided by the NLopt library[62]; Supplementary Section 2a for more details). This optimization algorithm can be readily applied to multitask problems by adopting the simple approach of optimizing a convex linear combination (scalarization) of multiple objectives. In particular, we can deploy this strategy to design reprogrammable architectures that can switch between multiple tasks. In this way, we can discover a range of solutions that explore the trade-off between distinct functionalities, thus identifying the Pareto front[16] (Supplementary Section 2b for more details). As a result, our design framework allows us to efficiently explore the large space of non-periodic architectures and converge to designs that—even if only locally optimal—encode one or multiple desired tasks.

Fabrication, characterization and testing

To evaluate the performance of the optimized designs, we fabricate them using three-dimensional (3D)-printed polylactic acid (PLA) units and thin polyester plastic shims with a rest length of $\ell_0 = 2.3$ mm (Fig. 1d). The mass density used in the 2D model is determined by measuring the mass of a representative sample and dividing it by the area of the PLA units, obtaining $\rho = 6.18$ kg m^{-2}. The mechanical behaviour of the hinges is systematically investigated by subjecting samples (comprising an array of 4×4 squares connected by these hinges) to tension, compression and shear. The experimental responses closely match the model predictions for $k_\ell = 120$ N mm^{-1}, $k_s = 1.19$ N mm^{-1} and $k_\theta = 1.50$ N mm. Furthermore, we find that the free oscillations of a square unit connected to the ground by a hinge align well with the model predictions for damping coefficients $c_u = 2.9 \times 10^{-2}$ kg s^{-1} and $c_\theta = 1.2 \times 10^{-7}$ kg m^2 s^{-1}. In addition, the contact stiffness is assumed to be $k_c = k_\theta$, and contact angles are chosen as $\theta_{min} = -15°$ and $\theta_{cut\text{-}off} = -10°$ to prevent excessive overlap (contact) between the units. Finally, to ensure manufacturability, the minimum edge length

and vertex angle of the units are set as $e_{min} = 3$ mm and $\theta_{min}^{unit} = 30°$, respectively.

The fabricated structures are dynamically excited using a low-frequency shaker, and the response is recorded with a high-speed camera. A tracking algorithm based on digital image correlation is then used to reconstruct the displacement field of all the units and compare it to the simulated response (Supplementary Sections 4 and 5 for more details on fabrication and experimental methods).

Results

Energy focusing

To demonstrate our optimization-based approach, we first seek a metamaterial design that directs the kinetic energy provided by a large-amplitude pulse towards a target region Ω_t (Fig. 2a). To achieve this goal, we maximize the time integral of the kinetic energy at Ω_t:

$$J_{\Omega_t}(\mathbf{x}) = \sum_{i \in \Omega_t} \int_0^{t_f} \mathcal{T}_i(\mathbf{q}(t), \mathbf{x}) \, dt \qquad (7)$$

upon application of a pulse-like excitation on the left edge of the domain (region highlighted in red in Fig. 2a). In particular, we focus on a domain comprising 24×16 units, choose Ω_t to be four units located in the upper right part of the domain (region highlighted in green in Fig. 2a) and consider the following excitation signal:

$$u_{input}(t) = \frac{A}{2} \left(1 - \cos(2\pi f t)\right) \mathcal{H}(1/f - t)\mathcal{H}(t), \qquad (8)$$

where $A = 7.5$ mm and $f = 30$ Hz control the amplitude and width of the single pulse applied to the structure. Note that we choose the upper limit of integration in equation (7) to be $t_f = 2/f$, since we have found that larger values of integration time lead to a very comparable performance, while requiring a higher computational cost (Supplementary Fig. 10).

As shown in Fig. 2a, our optimization algorithm quickly alters the initial design comprising squares with a centre-to-centre spacing $s = 15$ mm and bias angle $\theta_0 = 25°$. Specifically, the algorithm modifies the geometry throughout the entire domain, and after approximately 60 iterations, identifies a design that concentrates $J_{\Omega_t}/t_f \approx 10$ mJ of energy in the target area. This represents a more than 400-fold enhancement compared with the initial periodic design, which focused around ~0.02 mJ in the target area. The optimized design features large quadrilaterals within the target region, surrounded by smaller units with a high aspect ratio, creating a structure that resembles an elastic resonator made of a high-inertia region embedded in a softer surrounding environment[63]. Additionally, a high-density region is situated just below the target, and low-density regions are positioned near the four corners of the domain. Note that these main geometric features are robust with respect to perturbation of the initial design (Supplementary Fig. 12). To understand the roles played by these regions, we analyse the temporal evolution of bending, shear and kinetic energies over this optimized design (Fig. 2b). At $t = 13$ ms, we find that the applied input primarily causes shearing of the ligaments in a straight region ahead of the excitation point. By $t = 34$ ms, the applied energy has transferred into both shear and bending energies, and the kinetic energy begins to focus at the target location. During this energy exchange, the high-density region below the target acts as a high-inertia reflection area where the kinetic energy gets distributed before being transferred towards the target region (Supplementary Video 1). This process continues until most of the kinetic energy is concentrated at the target, and very low strain energy is present elsewhere, resulting in a significant focusing event at the desired location ($t = 40$ ms). The exchange mechanism between the kinetic energy in the target area and the strain energy in the rest of the domain continues until all the energy is dissipated.
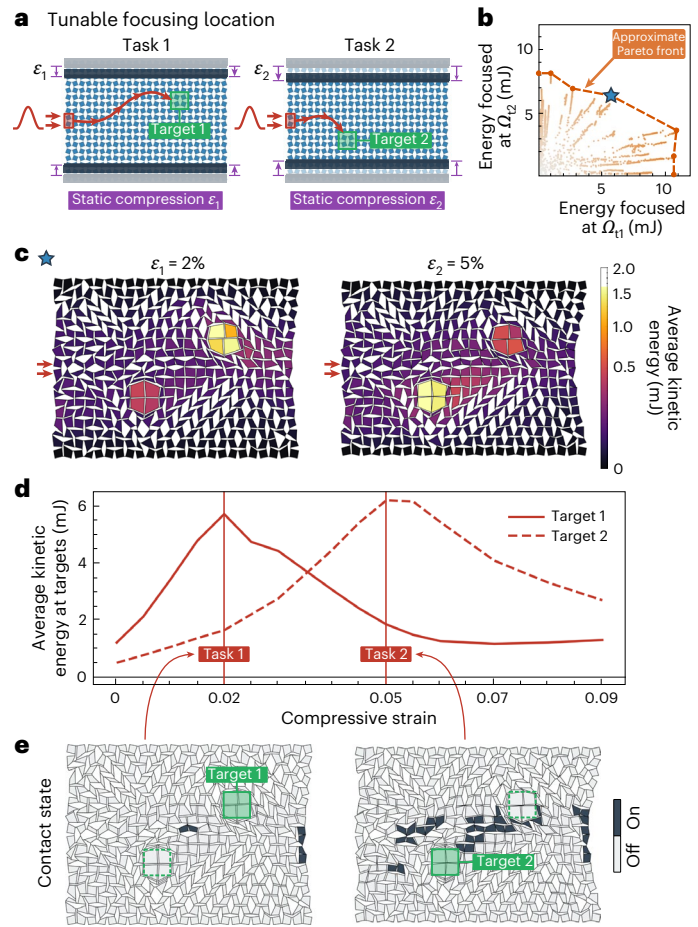

Fig. 3 | Reprogramming focusing location. a, On-the-fly tunability of the focusing location is achieved with a single architecture by harnessing static precompression (purple arrows). Left and right panels show tasks 1 and 2, respectively. **b**, $J_{\Omega_{t1}}^{(\varepsilon_1)}/t_f$ and $J_{\Omega_{t2}}^{(\varepsilon_2)}/t_f$ for all designs visited during optimization (each design point is coloured with a grey-to-orange gradient according to its distance from the origin). The resulting Pareto front is highlighted by the orange dashed line. **c**, Spatial distribution of time-averaged kinetic energy at the two desired compression levels, $\varepsilon_1 = 2\%$ (left) and $\varepsilon_2 = 5\%$ (right), for the best equal-performance design (highlighted by the blue star marker in **b**). **d**, Evolution of the average kinetic energy at the target regions Ω_{t1} and Ω_{t2} as a function of the applied precompression. **e**, Spatial distribution of contacts at the two desired compression levels, $\varepsilon_1 = 2\%$ (left) and $\varepsilon_2 = 5\%$ (right).

Next, we investigate the robustness of the optimized design with respect to different input pulses. Towards this end, we simulate its response upon the application of inputs with $A \in [0.1, 0.9]s = [1.5, 13.5]$ mm and $f \in [20, 55]$ Hz. In Fig. 2c we report the integral of the energy focused on the target region (Ω_t) compared with the rest of the domain ($\Omega \setminus \Omega_t$), $J_{\Omega_t}/J_{\Omega \setminus \Omega_t}$, for all the considered inputs. Notably, we observe that a comparable focusing performance is attained for inputs within a substantial region surrounding the input considered in the optimization (Supplementary Section 3a for more analysis on robustness). This robustness with respect to different excitation signals is a key prerequisite for experimental validation.

To experimentally demonstrate the focusing task, we fabricate the optimized design and dynamically excite it using a low-frequency shaker. In these experiments, the input excitation is extracted via digital image correlation tracking of the units connected to the shaker and then fed into our simulations for comparison. In Fig. 2d we report experimental and numerical snapshots at $t = 55$ ms when the structure is excited with the signal shown in the inset (with peak displacement ~9 mm). We find very good agreement between experiments and
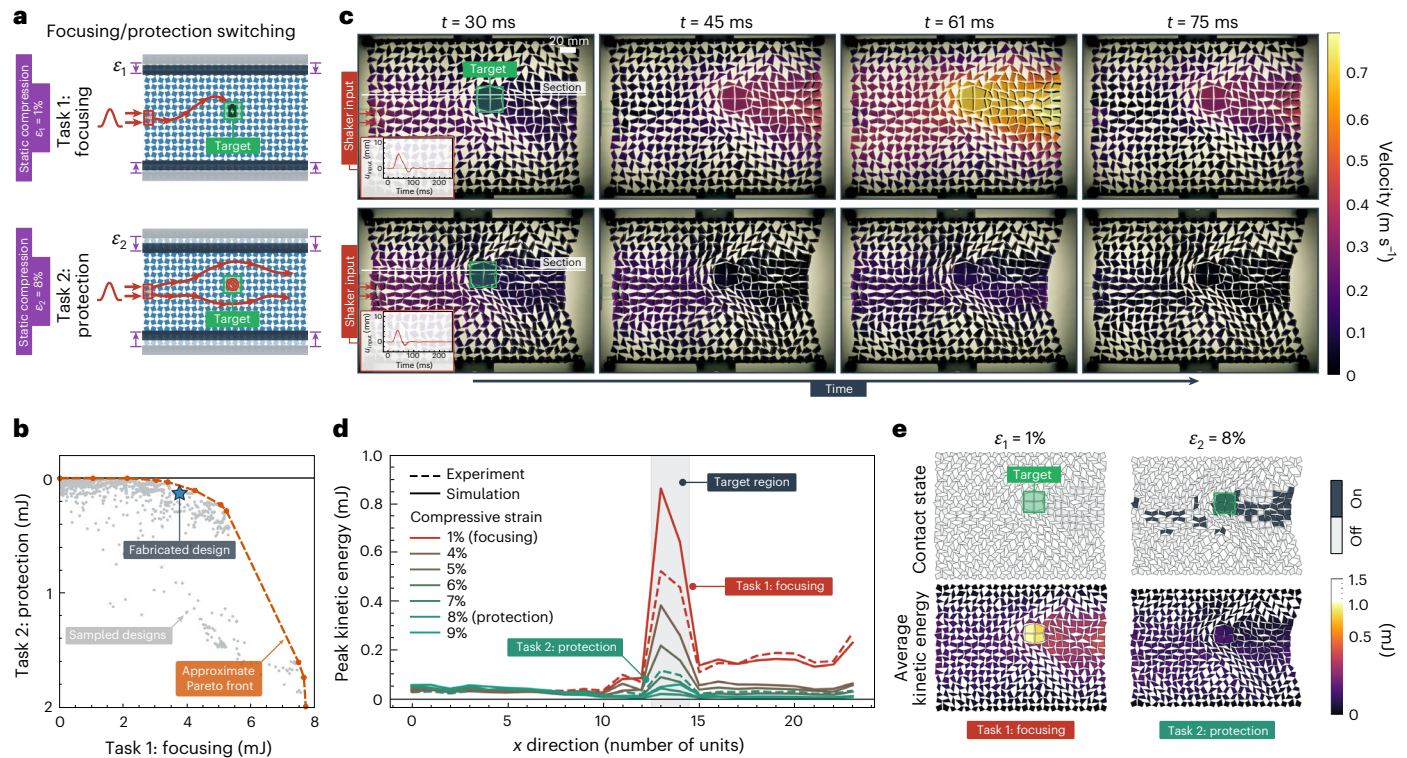
Fig. 4 | Reprogramming functionality. a, We search for a metamaterial architecture with the ability to maximize kinetic energy at a target location for an applied precompression of $\varepsilon_1 = 1\%$ (top) and minimize it for $\varepsilon_2 = 8\%$ (bottom). **b**, All designs visited during optimization (grey points) plotted in the objective space $J_{\Omega_t}^{(\varepsilon_1)}/t_f - J_{\Omega_t}^{(\varepsilon_2)}/t_f$. The resulting Pareto front is highlighted by the orange dashed line. **c**, Experimental snapshots of the fabricated design (marked by a blue star in **b**) when subject to a pulse-like excitation (shown in the insets) applied by a low-frequency shaker at $\varepsilon_1 = 1\%$ (top row) and $\varepsilon_2 = 8\%$ (bottom row). **d**, Peak kinetic energy profiles on a horizontal section across the target region (while line in **c**) for different levels of applied precompression. **e**, Simulated spatial distribution of contacts (top row) and corresponding kinetic energy distribution (bottom row) at the two desired compression levels, $\varepsilon_1 = 1\%$ (left column) and $\varepsilon_2 = 8\%$ (right column).

simulations, with a velocity magnitude that is largest in the target region. Furthermore, to assess the robustness of the focusing performance experimentally, we excite the optimized structure with input signals of varying amplitudes (Fig. 2e). In Fig. 2f, we present the peak kinetic energy, $\max_t \mathcal{T}_i$, along the white line in Fig. 2d for the three considered inputs. Notably, a clear concentration of kinetic energy exists at the specified target region (green shaded area), affirming the efficacy of the focusing mechanism.

This example of energy focusing design demonstrates how our strategy can discover geometries that channel energy towards a desired location without requirements on energy distribution anywhere else. More control over the spatial localization of energy can be achieved by generalizing this problem to multiple focusing locations. With such a strategy, we can design metamaterial architectures capable of splitting the input energy among specified target regions of space and doing so with a desired splitting ratio (Supplementary Section 3c). Additional results on the 'dual' problem of energy focusing at a single target area when the metamaterial is excited at different independent locations are reported in Supplementary Section 3d (Supplementary Fig. 5 and Supplementary Video 5). Furthermore, results demonstrating that our framework is applicable to arbitrary geometric spaces are reported in Supplementary Section 3f, showing the energy focusing design of a non-periodic metamaterial with a kagome-like topology (Supplementary Fig. 7 and Supplementary Video 6).

Reprogramming focusing location

In Fig. 2, we identified a design capable of concentrating the input energy at a specified location. Real-world challenges, however, often necessitate a tunability of the task. Crucially, we can harness the high

deformability of metamaterials to achieve such reprogrammability within a single architecture.

To illustrate this concept, we search for a metamaterial that can selectively focus energy in two distinct locations depending on the level of applied precompression. Specifically, we seek a 24 unit × 18 unit design that can focus energy in the target region Ω_{t1} when vertically precompressed by $\varepsilon_1 = 2\%$ and in the region Ω_{t2} when the precompression is increased to $\varepsilon_2 = 5\%$ (Fig. 3a). To identify such an architecture, we maximize the following objective function:

$$J = w_1 J_1 + w_2 J_2 \qquad (9)$$

where $J_i = J_{\Omega_{ti}}^{(\varepsilon_i)}$ ($i = 1, 2$) is given by equation (7) computed on the structure precompressed by ε_i, and $w_i \geq 0$ denotes the weight associated with the ith objective. Each objective $J_{ti}^{(\varepsilon_i)}$ is computed through a simulation involving two steps. In the initial step, a quasi-static compressive strain ε_i is applied by gradually displacing the top and bottom rows of the structure vertically. This is followed by a subsequent step where a dynamic pulse, defined by equation (8) with $A = 7.5$ mm and $f = 30$ Hz, is applied to the left edge (as indicated by the red arrows in Fig. 3a). To systematically sample the Pareto front of this multi-objective problem, we maximize equation (9) with $w_1 \in [0, 1]$ and $w_2 = 1 - w_1$ and track J_i for each design in the optimization. Note that, to enhance the resolution of the Pareto front, we consider five initial designs with $\theta_0 \in [15, 35]°$ for each weight combination (Supplementary Section 2b for more details on the Pareto sampling).

In Fig. 3b, we report $J_{\Omega_{t1}}^{(\varepsilon_1)}/t_f$ and $J_{\Omega_{t2}}^{(\varepsilon_2)}/t_f$ for all the designs visited during optimization (each design point is coloured with a grey-to-orange gradient according to its distance from the origin). The resulting Pareto front (orange dashed line) delineates a set of optimal, physically
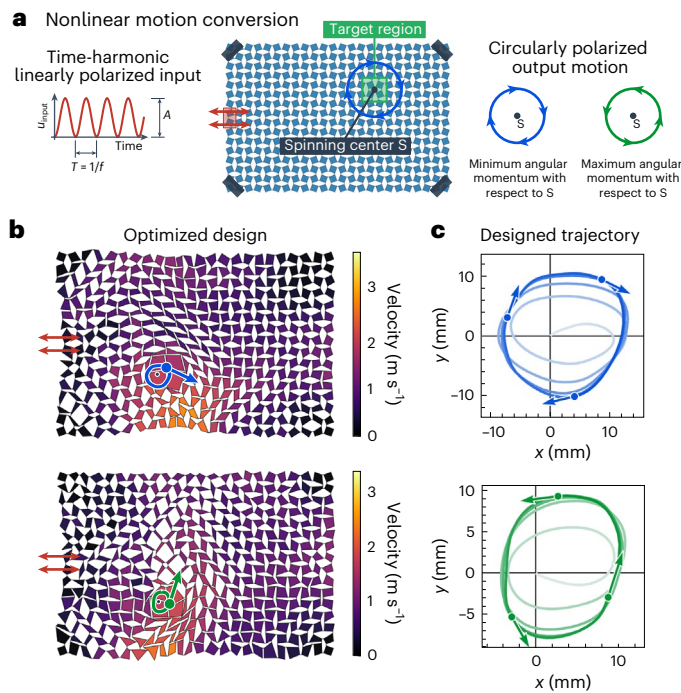
Fig. 5 | Nonlinear motion conversion. a, A linearly polarized harmonic input (left) can be converted to a circularly polarized motion (right) by a metamaterial architecture optimized for the angular momentum of a target region with respect to a specified point S (midpoint of the target region; middle). **b**, Two optimized designs (coloured according to the velocity map) for clockwise (top) and anticlockwise (bottom) output motion. **c**, Designed output motions generated by the designs shown in **b** coloured in blue (green) for clockwise (anticlockwise) direction.

realizable designs that exhibit diverse performance trade-offs in focusing at the two target locations. Additionally, it demonstrates that our optimization can always improve the performance of the starting design. In Fig. 3c, we focus on a design on the sampled Pareto front for which $J_{\Omega_{t1}}^{(\varepsilon_1)} \approx J_{\Omega_{t2}}^{(\varepsilon_2)}$ (highlighted by the blue star marker in Fig. 3b) and plot the time-averaged kinetic energy for $\varepsilon_1 = 2\%$ (left) and $\varepsilon_2 = 5\%$ (right). The two energy maps clearly show the switch between the two tasks at the desired precompression levels. Additionally, in Fig. 3d we report the time-averaged kinetic energy at Ω_{t1} (continuous red line) and Ω_{t2} (dashed red line) as a function of the applied precompression for $\varepsilon \in [0, 9]\%$. We find that as the applied precompressive strain is increased, the focused kinetic energy smoothly shifts from Ω_{t1} (continuous red line) to Ω_{t2} (dashed red line). Interestingly, we find that the optimization algorithm exploits contact between the quadrilateral units to achieve such a shift. As shown in Fig. 3e, at $\varepsilon = 2\%$, only two pairs of units are in contact. By contrast, at $\varepsilon = 5\%$, not only do more units get in contact, but they also form a contact chain that connects Ω_{t1} and Ω_{t2}. The added stiffness of this contact chain limits the motion of Ω_{t1} and ultimately causes the incoming energy to deflect towards the lower part of the domain, effectively exciting Ω_{t2} (Supplementary Video 2). Remarkably, the full differentiability of our model, which accounts for contact, allows us to discover such a contact-based switching mechanism in an automated fashion.

Reprogramming functionality

The results of Fig. 3 demonstrate that our design strategy can discover metamaterials with a programmable focusing location. Here we pose a more challenging question: is our design space rich enough to allow a single metamaterial structure to perform antagonistic tasks? To answer this question, we deploy our design strategy to search for a

metamaterial architecture with the ability to maximize kinetic energy at a target location Ω_t for an applied precompression of $\varepsilon = \varepsilon_1$ and to minimize it for $\varepsilon = \varepsilon_2$ (Fig. 4a). This multitask problem is solved by maximizing the objective function of equation (9) with $\Omega_{t1} = \Omega_{t2} = \Omega_t$, and with $w_1 \in [0, 1]$ and $w_2 = w_1 - 1 \in [-1, 0]$ for the tasks of energy maximization and minimization, respectively. Figure 4 displays results for a domain consisting of 24 units × 18 units under identical excitation as that considered in Fig. 3, with $\varepsilon_1 = 1\%$ and $\varepsilon_2 = 8\%$. The Pareto front sampling for this problem is shown in Fig. 4b. The majority of the explored designs (grey markers) demonstrate a combination of low-focusing and high-protection capabilities. This suggests that, within the metamaterial design space considered and for the considered target location, it is comparatively easier to design for energy minimization than for energy maximization.

To verify the robustness of the identified optimal designs, we fabricate and test a design on the Pareto front with a focusing-to-protection performance ratio of about 25 (that is, $J_{\Omega_t}^{(\varepsilon_1)} \approx 25 J_{\Omega_t}^{(\varepsilon_2)}$; blue star marker in Fig. 4b). We use linear stages connected to the units at the top and bottom rows to apply the desired level of precompression and then dynamically excite the preloaded sample using a low-frequency shaker. In Fig. 4c we report experimental snapshots of the sample precompressed by $\varepsilon_1 = 1\%$ (top) and $\varepsilon_2 = 8\%$ (bottom) after dynamic excitation, with each quad coloured according to the measured velocity magnitude. In full agreement with the predictions of the model, we find a high velocity region around the target when the sample is precompressed by ε_1 with a peak of 0.72 m s^{-1} observed at the target at $t = 61$ ms (Supplementary Video 3 reports the experimental and simulated dynamic response of this optimized structure). By contrast, the velocity remains lower than 0.41 m s^{-1} within the entire domain when the structure is precompressed by ε_2. The efficiency of the design in transitioning from focusing to protection as the applied precompression increases is further apparent in Fig. 4d. Here we plot the peak kinetic energy extracted along a horizontal section across the target region for varying levels of applied precompression. In addition to a good agreement between experiments (dashed lines) and simulations (solid lines), the data indicate a consistent decrease in peak kinetic energy within the target region (shaded grey area) as the applied precompression increases. Notably, for $\varepsilon > 8\%$, the peak kinetic energy is markedly low. In this instance as well, we observe that the optimization algorithm uses contact to switch between the two tasks (Fig. 4e). At $\varepsilon = \varepsilon_1$, no units are in contact. However, at $\varepsilon = \varepsilon_2$, the units in the target region and numerous units behind it come into contact, resulting in a 'jammed' state. We can interpret the formation of these jammed regions as the attempt of the optimization to locally tune the effective mass density and stiffness to effectively engineer a switch in the dynamic response. In fact, the jammed areas correspond to the regions that, compared with the rest of the domain, undergo a sharp transition from a high kinetic energy at ε_1 to a low kinetic energy response at ε_2 (Fig. 4e, bottom row).

Discussion and outlook

This study has introduced an automated design framework for identifying non-periodic metamaterials capable of intricate nonlinear dynamic tasks. Crucially, the resulting optimized architectures feature non-trivial geometries that could not be guessed or intuited a priori, highlighting the potential of our design framework for discovering material responses in an automated fashion. Moreover, we have demonstrated the extensibility of this framework to include reprogrammability, facilitating encoding and switching between multiple tasks by leveraging the inherent flexibility of the structures.

While our emphasis in this work has centred on converting large-amplitude pulses into controlled energy flow within metamaterial domains, the framework can be readily extended to accommodate various types of excitation signals and to identify architectures that support a broad spectrum of functionalities. As an example, in Fig. 5 we consider the design of a metamaterial that transforms a linearly polarized

large-amplitude harmonic input into an approximately circularly polarized motion at a specified target region. An architecture capable of anticlockwise motion is identified by maximizing the angular momentum of a target region with respect to a desired point. By contrast, achieving clockwise motion involves minimizing the angular momentum (Supplementary Section 3e for details, and Supplementary Video 4).

All together, the results presented here indicate that the proposed framework holds promise in identifying metamaterials capable of complex transient as well as steady-state dynamic behaviours in response to simple actuation inputs. We envision this paving the way for matter that can transform simple applied excitations into complex motions in specific regions. The reprogrammability of the behaviours could be further augmented by enabling simple task selection strategies through changes in excitation frequency, or variations in loading location. In summary, we envisage the resulting design paradigm being able to turn mechanical metamaterials into a rich robotic matter platform for generating soft material embodiments with reconfigurable functionalities. Our platform can facilitate the development of adaptable robotic systems, where part of the 'intelligence' is integrated directly into their body, thereby reducing the need for actuators and simplifying complex electronic controls.

Building on these capabilities, our platform can lead to impactful applications in robotics, tunable vibration control and large-amplitude impact mitigation, as well as energy harvesting in highly deformable structures.

Online content

Any methods, additional references, Nature Portfolio reporting summaries, source data, extended data, supplementary information, acknowledgements, peer review information; details of author contributions and competing interests; and statements of data and code availability are available at https://doi.org/10.1038/s41563-024-02008-6.

References

1. Ma, G. & Sheng, P. Acoustic metamaterials: from local resonances to broad horizons. *Sci. Adv.* **2**, e1501595 (2016).
2. Zangeneh-Nejad, F., Sounas, D. L., Alù, A. & Fleury, R. Analogue computing with metamaterials. *Nat. Rev. Mater.* **6**, 207–225 (2021).
3. Silva, A. et al. Performing mathematical operations with metamaterials. *Science* **343**, 160–163 (2014).
4. Zhang, S., Xia, C. & Fang, N. Broadband acoustic cloak for ultrasound waves. *Phys. Rev. Lett.* **106**, 024301 (2011).
5. Stenger, N., Wilhelm, M. & Wegener, M. Experiments on elastic cloaking in thin plates. *Phys. Rev. Lett.* **108**, 014301 (2012).
6. Xue, Y. & Zhang, X. Self-adaptive acoustic cloak enabled by soft mechanical metamaterials. *Extreme Mech. Lett.* **46**, 101347 (2021).
7. Deng, B., Raney, J. R., Bertoldi, K. & Tournat, V. Nonlinear waves in flexible mechanical metamaterials. *J. Appl. Phys.* **130**, 040901 (2021).
8. Patil, G. U. & Matlack, K. H. Review of exploiting nonlinearity in phononic materials to enable nonlinear wave responses. *Acta Mech.* **233**, 1–46 (2022).
9. Nadkarni, N., Arrieta, A. F., Chong, C., Kochmann, D. M. & Daraio, C. Unidirectional transition waves in bistable lattices. *Phys. Rev. Lett.* **116**, 244501 (2016).
10. Raney, J. R. et al. Stable propagation of mechanical signals in soft media using stored elastic energy. *Proc. Natl Acad. Sci. USA* **113**, 9722–9727 (2016).
11. Yasuda, H. et al. Origami-based impact mitigation via rarefaction solitary wave creation. *Sci. Adv.* **5**, eaau2835 (2019).
12. Jin, L. et al. Guided transition waves in multistable mechanical metamaterials. *Proc. Natl Acad. Sci. USA* **117**, 2319–2325 (2020).
13. Zaiser, M. & Zapperi, S. Disordered mechanical metamaterials. *Nat. Rev. Phys.* **5**, 679–688 (2023).
14. Bendsøe, M. P. & Sigmund, O. *Topology Optimization: Theory, Methods, and Applications* (Springer, 2004).
15. Sigmund, O. & Maute, K. Topology optimization approaches. *Struct. Multidiscip. Optim.* **48**, 1031–1055 (2013).
16. Osanov, M. & Guest, J. K. Topology optimization for architected materials design. *Annu. Rev. Mater. Res.* **46**, 211–233 (2016).
17. Wu, J., Sigmund, O. & Groen, J. P. Topology optimization of multi-scale structures: a review. *Struct. Multidiscip. Optim.* **63**, 1455–1480 (2021).
18. van Dijk, N. P., Maute, K., Langelaar, M. & van Keulen, F. Level-set methods for structural topology optimization: a review. *Struct. Multidiscip. Optim.* **48**, 437–472 (2013).
19. Sigmund, O. & Jensen, J. S. Systematic design of phononic band-gap materials and structures by topology optimization. *Philos. Trans. R. Soc. A* **361**, 1001–1019 (2003).
20. Liu, W., Yoon, G. H., Yi, B., Choi, H. & Yang, Y. Controlling wave propagation in one-dimensional structures through topology optimization. *Comput. Struct.* **241**, 106368 (2020).
21. Dong, H. W., Zhao, S. D., Wang, Y. S. & Zhang, C. Topology optimization of anisotropic broadband double-negative elastic metamaterials. *J. Mech. Phys. Solids* **105**, 54–80 (2017).
22. Li, Y. F., Meng, F., Zhou, S., Lu, M. H. & Huang, X. Broadband all-angle negative refraction by optimized phononic crystals. *Sci. Rep.* **7**, 7445 (2017).
23. He, J. & Kang, Z. Achieving directional propagation of elastic waves via topology optimization. *Ultrasonics* **82**, 1–10 (2018).
24. Capers, J. Inverse design of thin-plate elastic wave devices. *Phys. Rev. Appl.* **20**, 034064 (2023).
25. Bösch, C., Dubček, T., Schindler, F., Fichtner, A. & Serra-Garcia, M. Discovery of topological metamaterials by symmetry relaxation and smooth topological indicators. *Phys. Rev. B* **102**, 241404 (2020).
26. Jensen, J. S. Topology optimization of dynamics problems with Padé approximants. *Int. J. Numer. Methods Eng.* **72**, 1605–1630 (2007).
27. Boddeti, N., Tang, Y., Maute, K., Rosen, D. W. & Dunn, M. L. Optimal design and manufacture of variable stiffness laminated continuous fiber reinforced composites. *Sci. Rep.* **10**, 16507 (2020).
28. Wu, K., Sigmund, O. & Du, J. Design of metamaterial mechanisms using robust topology optimization and variable linking scheme. *Struct. Multidiscip. Optim.* **63**, 1975–1988 (2021).
29. Fraternali, F., Porter, M. A. & Daraio, C. Optimal design of composite granular protectors. *Mech. Adv. Mater. Struct.* **17**, 1–19 (2009).
30. Oliveri, G. & Overvelde, J. T. Inverse design of mechanical metamaterials that undergo buckling. *Adv. Funct. Mater.* **30**, 1909033 (2020).
31. Bessa, M. A., Glowacki, P. & Houlder, M. Bayesian machine learning in metamaterial design: fragile becomes supercompressible. *Adv. Mater.* **31**, 1904845 (2019).
32. Mo, C., Perdikaris, P. & Raney, J. R. Accelerated design of architected materials with multifidelity Bayesian optimization. *J. Eng. Mech.* **149**, 04023032 (2023).
33. Martins, J. R. R. A. & Ning, A. *Engineering Design Optimization* 1st edn (Cambridge Univ. Press, 2021).
34. Yang, Z., Yu, C. H. & Buehler, M. J. Deep learning model to predict complex stress and strain fields in hierarchical composites. *Sci. Adv.* **7**, eabd7416 (2021).
35. Deng, B. et al. Inverse design of mechanical metamaterials with target nonlinear response via a neural accelerated evolution strategy. *Adv. Mater.* **34**, 2206238 (2022).
36. Lew, A. J., Jin, K. & Buehler, M. J. Designing architected materials for mechanical compression via simulation, deep learning, and experimentation. *npj Comput. Mater.* **9**, 80 (2023).

37. Cheng, X. et al. Programming 3D curved mesosurfaces using microlattice designs. *Science* **379**, 1225–1232 (2023).

38. Silver, D. et al. A general reinforcement learning algorithm that masters chess, shogi, and Go through self-play. *Science* **362**, 1140–1144 (2018).

39. Raissi, M., Perdikaris, P. & Karniadakis, G. E. Physics-informed neural networks: a deep learning framework for solving forward and inverse problems involving nonlinear partial differential equations. *J. Comput. Phys.* **378**, 686–707 (2019).

40. Fawzi, A. et al. Discovering faster matrix multiplication algorithms with reinforcement learning. *Nature* **610**, 47–53 (2022).

41. Baydin, A. G., Pearlmutter, B. A., Radul, A. A. & Siskind, J. M. Automatic differentiation in machine learning: a survey. *J. Mach. Learn. Res.* **18**, 1–43 (2018).

42. Bradbury, J. et al. JAX: composable transformations of Python+NumPy programs (Google, 2018).

43. Schoenholz, S. S. & Cubuk, E. D. JAX, M.D.: a framework for differentiable physics. In *Proc. 34th International Conference on Neural Information Processing Systems* 11428–11441 (Curran Associates, 2020).

44. Minkov, M. et al. Inverse design of photonic crystals through automatic differentiation. *ACS Photon.* **7**, 1729–1741 (2020).

45. Goodrich, C. P., King, E. M., Schoenholz, S. S., Cubuk, E. D. & Brenner, M. P. Designing self-assembling kinetics with differentiable statistical physics models. *Proc. Natl Acad. Sci. USA* **118**, e2024083118 (2021).

46. Akerson, A. Optimal structures for failure resistance under impact. *J. Mech. Phys. Solids* **172**, 105172 (2023).

47. Wang, F. Systematic design of 3D auxetic lattice materials with programmable Poisson's ratio for finite strains. *J. Mech. Phys. Solids* **114**, 303–318 (2018).

48. Dou, S., Strachan, B. S., Shaw, S. W. & Jensen, J. S. Structural optimization for nonlinear dynamic response. *Philos. Trans. R. Soc. A* **373**, 20140408 (2015).

49. Li, L. L. et al. Tailoring the nonlinear response of MEMS resonators using shape optimization. *Appl. Phys. Lett.* **110**, 081902 (2017).

50. Oktay, D., Mirramezani, M., Medina, E. & Adams, R. P. Neuromechanical autoencoders: learning to couple elastic and neural network nonlinearity. In *Proc. International Conference on Learning Representations* (ICLR, 2023).

51. Grima, J. N. & Evans, K. E. Auxetic behavior from rotating squares. *J. Mater. Sci. Lett.* **19**, 1563–1565 (2000).

52. Cho, Y. et al. Engineering the shape and structure of materials by fractal cut. *Proc. Natl Acad. Sci. USA* **111**, 17390–17395 (2014).

53. Celli, P. et al. Shape-morphing architected sheets with non-periodic cut patterns. *Soft Matter* **14**, 9744–9749 (2018).

54. Coulais, C., Kettenis, C. & van Hecke, M. A characteristic length scale causes anomalous size effects and boundary programmability in mechanical metamaterials. *Nat. Phys.* **14**, 40–44 (2018).

55. Czajkowski, M., Coulais, C., van Hecke, M. & Rocklin, D. Z. Conformal elasticity of mechanism-based metamaterials. *Nat. Commun.* **13**, 211 (2022).

56. Zheng, Y., Niloy, I., Tobasco, I., Celli, P. & Plucinsky, P. Modelling planar kirigami metamaterials as generalized elastic continua. *Proc. R. Soc. A* **479**, 20220665 (2023).

57. Deng, B., Mo, C., Tournat, V., Bertoldi, K. & Raney, J. R. Focusing and mode separation of elastic vector solitons in a 2D soft mechanical metamaterial. *Phys. Rev. Lett.* **123**, 024101 (2019).

58. Yasuda, H., Korpas, L. M. & Raney, J. R. Transition waves and formation of domain walls in multistable mechanical metamaterials. *Phys. Rev. Appl.* **13**, 054067 (2020).

59. Deng, B., Raney, J. R., Tournat, V. & Bertoldi, K. Elastic vector solitons in soft architected materials. *Phys. Rev. Lett.* **118**, 204102 (2017).

60. Dormand, J. & Prince, P. A family of embedded Runge–Kutta formulae. *J. Comput. Appl. Math.* **6**, 19–26 (1980).

61. Svanberg, K. The method of moving asymptotes—a new method for structural optimization. *Int. J. Numer. Methods Eng.* **24**, 359–373 (1987).

62. Johnson, S. G. The NLopt nonlinear-optimization package. *GitHub* http://github.com/stevengj/nlopt (2007).

63. Liu, Z. et al. Locally resonant sonic materials. *Science* **289**, 1734–1736 (2000).

Methods

Differentiable simulation

The core element to our strategy is a custom-developed simulation environment for discrete mechanical metamaterials implemented in JAX (ref. 42). This implementation allows for arbitrary parameterization of the following:

(1) 2D geometric patterns comprising rigid polygons connected by deformable ligaments; the examples of non-periodic quads and non-periodic kagome patterns are detailed in Supplementary Section 1

(2) Elastic couplings defining the mechanical response of the ligaments, for example, the strain energy given by equation (1)

(3) External loading $\mathbf{f}_{ext}$ appearing at the right-hand side of the equation of motion, equation (5)

As all these ingredients are implemented in JAX, the resulting mapping between geometry, ligament parameters, loading parameters and the response of the system is differentiable. This allows us to derive gradients of the objective function in an automated fashion. In particular, reverse-mode AD has been used in all the optimizations presented in this work. Gradients of the design constraints (lower bounds on the edge lengths and angles of the units) are also computed using the same technique. The computation of all of these gradients is then coupled to the Method of Moving Asymptotes[61] to perform design updates. In the case of multitask problems, we adopt the scalarization method. More details on multitask optimization and Pareto front analysis are provided in Supplementary Section 2. Information on the sensitivity of the optimized design with respect to loading parameters and initial design are detailed in Supplementary Section 3a,i.

Fabrication

The structures used in all the experiments are fabricated via a custom assembly process involving 3D printing of PLA units and laser cutting of plastic shims. More details about the fabrication process are provided in Supplementary Section 4.

Experimental methods

Parameter identification. The stiffness parameters characterizing the flexible ligaments have been identified via uniaxial quasi-static testing of small 4 unit × 4 unit square samples subject to tension, compression and shear. The fitted stiffness parameters are then validated against the response of an 8 unit × 8 unit quad random sample. The viscous damping coefficients are estimated via the logarithmic decrement method on free oscillating samples of a square unit connected to ground by a flexible ligament. More details on the characterization experiments and procedures are provided in Supplementary Section 5a.

Dynamic testing and video analysis. The fabricated structures are excited using a low-frequency shaker, and their dynamics are recorded by a high-speed camera. A custom image processing code based on digital image correlation is used to track the motion of the units. More details on the experimental procedures used for dynamic testing and the image tracking analysis are summarized in Supplementary Section 5b,c.

Data availability

All the data necessary to reproduce the findings in this work are available via Zenodo at https://doi.org/10.5281/zenodo.12823471 (ref. 64).

Code availability

All the source code developed for this work is available on GitHub at https://github.com/bertoldi-collab/DifFlexMM.

References

64. Bordiga, G. et al. Automated discovery of reprogrammable nonlinear dynamic metamaterials. *Zenodo* https://doi.org/10.5281/zenodo.12823471 (2024).

Author contributions

G.B., E.M., V.T. and K.B. designed the research. G.B. wrote the simulation and optimization codes. S.J. designed the fabrication process. S.J., G.B. and E.M. performed the fabrication. V.T., S.J. and G.B. performed experiments. G.B., C.B. and E.M. performed simulations and optimizations. G.B., E.M., S.J., C.B., R.P.A., V.T. and K.B. analysed data and wrote the paper.

Competing interests

The authors declare no competing interests.

Additional information

Supplementary information The online version contains supplementary material available at https://doi.org/10.1038/s41563-024-02008-6.

Correspondence and requests for materials should be addressed to Katia Bertoldi.

Peer review information *Nature Materials* thanks Hongsheng Chen, Michael Zaiser and the other, anonymous, reviewer(s) for their contribution to the peer review of this work.

Reprints and permissions information is available at www.nature.com/reprints.